Thermal Imaging Performance of the TIR onboard the Hayabusa2 Spacecraft

Takehiko Arai · Tomoki Nakamura · Satoshi Tanaka · Hirohide Demura · Yoshiko Ogawa · Naoya Sakatani · Yamato Horikawa · Hiroki Senshu · Tetsuya Fukuhara · Tatsuaki Okada

T. Arai Center for Global Environmental Research, National Institute for Environmental Studies, 16-2 Onogawa, Tsukuba, Ibaraki 305-8506, JAPAN E-mail: arai.takehiko@nies.go.jp

T. Nakamura Department of Earth Science, Tohoku University, Sendai, JAPAN

S. Tanaka · T. Okada Institute of Space and Astronautical Science, Japan Aerospace eXploration Agency, Sagamihara, JAPAN

H. Demura · Y. Ogawa Center for Advanced Information Science and Technology, The University of Aizu, Aizu- Wakamatsu, JAPAN

N. Sakatani Department of Physics, Meiji University, Kawasaki, JAPAN

Y. Horikawa Department of Space and Astronautical Science, School of Physical Sciences, Graduate University for Advanced Studies, Sagamihara, JAPAN

H. Senshu Planetary Exploration Research Center, Chiba Institute of Technology, Tsudanuma, JAPAN

T. Fukuhara Department of Physics, Rikkyo University, Ikebukuro, JAPAN

The thermal infrared imager (TIR) is a thermal infrared camera onboard the Hayabusa2 spacecraft. The TIR will perform thermography of a C-type asteroid, 162173 Ryugu (1999 JU$_3$), and estimate its surface physical properties, such as surface thermal emissivity ε, surface roughness, and thermal inertia Γ , through remote in-situ observations in 2018 and 2019. In prelaunch tests of the TIR, detector calibrations and evaluations, along with imaging demonstrations, were performed. The present paper introduces the experimental results of a prelaunch test conducted using a large-aperture collimator in conjunction with the TIR under atmospheric conditions. A blackbody source, controlled at constant temperature, was measured using the TIR in order to construct a calibration curve for obtaining temperatures from observed digital data. As a known thermal emissivity target, a sandblasted black almite plate warmed from the back using a flexible heater was measured by the TIR in order to evaluate the accuracy of the calibration curve. As an analog target of a C-type asteroid, carbonaceous chondrites (50 mm × 2 mm in thickness) were also warmed from the back and measured using the TIR in order to clarify the imaging performance of the TIR. The calibration curve, which was fitted by a specific model of the Planck function, allowed for conversion to the target temperature within an error of 1°C (3σ) for the temperature range of 30 to 100°C. The observed temperature of the black almite plate was consistent with the temperature measured using type K

thermocouples, within the accuracy of temperature conversion using the calibration curve when the temperature variation exhibited a random error of 0.3°C (1σ) for each pixel at a target temperature of 50°C. The TIR could resolve the fine surface structure of meteorites, including cracks and pits with the specified field of view of 0.05° (328 × 248 pixels). There were spatial distributions with a temperature variation of 3°C at the setting temperature of 50°C in the thermal images obtained by the TIR. If the spatial distribution of the temperature is caused by the variation of the thermal emissivity, including the effects of the surface roughness, the difference of the thermal emissivity Δε is estimated to be approximately 0.08, as calculated by the Stefan-Boltzmann law. Otherwise, if the distribution of temperature is caused by the variation of the thermal inertia, the difference of the thermal inertia ΔΓ is calculated to be approximately 150 $Jm^{-2}s^{0.5}K^{-1}$, based on a simulation using a 20-layer model of the heat balance equation. The imaging performance of the TIR based on the results of the meteorite experiments indicates that the TIR will allow for resolving the spatial distribution of thermal emissivity and thermal inertia of the asteroid surface within accuracies of Δε ~= 0.02 and ΔΓ ~= 20 $Jm^{-2}s^{0.5}K^{-1}$, respectively. However, the effects of the thermal emissivity and thermal inertia will be degenerated in thermal images of the TIR. Therefore, the TIR will observe the same areas of the asteroid surface numerous times (>10 times, in order to ensure statistical significance), and this will allow for determining both the parameters of the surface thermal emissivity and the thermal inertia by least-squares fitting to a thermal model of Ryugu.

1 Introduction

The thermal infrared imager (TIR) is a thermal infrared camera on board the Hayabusa2 spacecraft that will perform thermography of the asteroid Ryugu and estimate the thermo-physical properties of its surface materials through in- situ observations in 2018 and 2019 (Okada et al., 2014). The TIR is the same in design as the long-wave infrared camera (LIR) on board the AKATSUKI Venus climate orbiter (Fukuhara et al., 2011). The Hayabusa2 spacecraft, which has the goal of returning an asteroid sample to Earth (Tsuda et al., 2013), was launched by the 26th H-IIA launch vehicle from the Tanegashima Space Center on December 3, 2014.

The detector of the TIR is an uncooled micro-bolometer array that is based on a commercial model (320A NEC Inc. Co.). The TIR remotely observes the temperature of the target by converting the thermal radiation emitted by the target to an electric signal by measuring the resistance changes of the micro-bolometer. The TIR captures a 328 × 248 pixel image and has a spatial resolution of ~ 0.05 /pixel with a field of view (FOV) of 16 × 12 . The band- pass filter of the TIR limits the range of detection of the thermal radiation emitted from the target to wavelengths of 8 to 12 μm (Okada et al., 2016).

The target asteroid, 162173 Ryugu (1999 JU$_3$), is a C-type near-Earth asteroid classified by Bus taxonomy (Bus and Binzel, 2002), which is considered to be a parent body of carbonaceous chondrites. Ryugu is approximately 0.8 km in size, and its rotation period is 7.6 hours (Mu˙ller et al., 2011). The spectrum features of Ryugu observed using a ground-based telescope exhibit a variation in the absorption band near the wavelength of 0.7 μm, which implies that Ryugu has experienced aqueous alteration of its surface (Vilas, 2008). However, no absorption spectra have been reported by Lazzaro et al., (2013). Thus, each area of Ryugu may have several features, so that in-situ observation by Hayabusa2 is significant.

Creating a global map of thermal inertia for the asteroid surface is a primary goal of the TIR. The thermal inertia Γ , which represents the resistance to temperature change of a target, depends on the physical and thermal properties of the target surface and can be expressed as follows:

$$\Gamma = \sqrt{\rho c_p \kappa}, \tag{1}$$

where ρ is the density, c_p is the specific heat, and κ is the thermal conductivity. The thermal inertia of Ryugu has been observed with ground-based telescopes and space-based telescopes, as follows: $\Gamma \geq 500$ $Jm^{-2}s^{0.5}K^{-1}$ (Hasegawa et al., 2008), $\Gamma \sim = 200$ to 600 $Jm^{-2}s^{0.5}K^{-1}$ (Mu˙ller et al., 2011), and $\Gamma \sim = 150$ to 700 ± 200 $Jm^{-2}s^{0.5}K^{-1}$ (Campins et al., 2009). The differences in these results may indicate that the surface of Ryugu is locally formed of various components, such as boulders, pebble rocks, sands, and regolith. Thermal inertia affects the peak shift of diurnal time at the maximum temperature of the asteroid surface. The Yarkovsky effect states that the local distribution of thermal inertia is critical to orbital changes of the asteroid (Bottke et al., 2006). As such, the TIR will estimate the spatial distribution of the thermal inertia to a degree sufficient to resolve the thermal properties of the various asteroid components. The required accuracy for the observation of the TIR is $\Delta\Gamma \sim = 100$ $Jm^{-2}s^{0.5}K^{-1}$ of the order (Table 1 in Okada et al., 2016).

The surface thermal emissivity of the asteroid is also an important target of the TIR because this quantity includes surface information, such as surface composition and surface roughness. The thermal emissivity ε of radiative targets is derived using the Stefan-Boltzmann law, as follows:

$$\epsilon = \frac{E}{\sigma T^4},\tag{2}$$

where E is the radiant existence (Wm^{-2}) emitted from the target, $\sigma = 5.67 \times 10^{-8}$ ($Wm^{-2}K^{-4}$) is the Stefan-Boltzmann constant, and T (K) is the temperature of the target. In asteroid observations, surface terrain can generate shadows due to solar light, and multiple radiation sources can result in surface temperature variation (Rozitis and Green, 2011). Under the spatial resolution of the TIR, the rough terrain, referred to herein as "surface roughness", changes the surface thermal emissivity. The thermal emissivity of meteorites has generally been measured in terms of spectral reflectance, which is then translated to thermal emissivity using Kirchhoff's law of thermal radiation (1-reflectance). The spectral reflectance of carbonaceous chondrites has been reported by Baldridge et al. (2009), and the mean value calculated for the reflectance to the thermal emissivity in the TIR band-pass wavelength range of 8 to 12 μm is approximately 0.99. This value implies that the thermal emissivity of the carbonaceous chondrites is mostly "black". On the other hand, the geometric albedo of Ryugu, as observed by the Spitzer Space Tele- scope (Campins et al., 2009), is 0.07±0.01. If the thermal emissivity varies from 0.92 to 0.94, as calculated by Kirchhoff's law, the surface temperature will change by approximately 2˚C for the target temperature range of 0 to 100˚C, as estimated using Eq. (2).

The spatial distribution of surface thermal emissivity and the thermal inertia changes the surface temperature of the asteroid. Therefore, the TIR must distinguish the effects of both surface thermal emissivity and thermal inertia in order to clarify the surface properties of the asteroid based on the thermal imaging performance of the TIR. The primary goals of the present study are to clarify the imaging performance of the TIR through the calibration, evaluation, and demonstration of prelaunch tests and to discuss the observation of the surface thermal emissivity and the thermal inertia of the asteroid.

2 Calibration using a blackbody source

The purpose of this calibration test of the TIR is to generate a calibration curve from observed digital data to obtain target temperatures.

2.1 Experimental configuration

Prelaunch calibrations of the TIR were performed using a vacuum chamber, an oil bath, cavity blackbody sources, and a collimator in the temperature range of -40 to 150°C (Okada et al., 2016). In the present study, the calibration of the TIR was performed using the best-focused images of a blackbody source installed in the collimator (METS-VS-8-2.9, CI-Systems) in the temperature range of 30 to 100°C, as shown in Fig. 1. The collimator had an aperture of 0.2 m, a focal length of 1.0 m, a field of view of 2.9°, and a measurable wavelength of 0.4 to 15 μm (SR800R, CI-Systems). Moreover, the thermal emissivity of the blackbody source was measured using commercial infrared cameras: AVIO G100 and AVIO G100EX (Nippon Avionics Co., Ltd.). The resulting thermal emissivity of the blackbody source had a value of 0.99±0.01. The attenuation of thermal radiation from the blackbody source due to atmospheric absorption is approximately zero in this wavelength range because the focal length was short at 1 m. Thus, the atmospheric attenuation is negligible in this configuration, but in the observation of distant targets, must consider the precipitable water vapor between the detector and the targets. Thermal radiation emitted from ambient air is negligible because outer and inner radiation of the TIR is suppressed by thermal chopping which is onboard data reduction of the TIR to subtract shutter images from target images (Okada et al., 2016).

2.2 Calibration curve

The TIR measures the radiance emitted from targets and estimates the temperatures from the observed radiance. The spectral radiance emitted from a blackbody $B(\lambda,T)$ $(\mathrm{Wsr^{-1}m^{-2}})$ as a function of wavelength λ (m) and temperature T (K) is given by the Planck function as follows:

$$B(\lambda, T) = \frac{2hc^2}{\lambda^5} \frac{1}{\exp\left(\frac{hc}{\lambda k_B T}\right) - 1}.$$

Here, $h = 6.63 \times 10^{34}$ $(\mathrm{m^2 kg\ s^{-1}})$ is the Planck constant, $k_B = 1.38 \times 10^{-23}$ $(\mathrm{m^2 kg\ s^{-2}\ K^{-1}})$ is the Boltzmann constant, and $c = 2.99792 \times 10^8$ $(\mathrm{ms^{-1}})$ is the speed of light. The observed radiant flux per area F(T) $(\mathrm{Wm^{-2}})$ over all wavelengths with the TIR is limited by the response function of the TIR $R(\lambda)$, such as the detection

efficiency of the bolometer, the transmittance of the band-pass filter, and the transmittance of the germanium lens (Fig. 11 of Okada et al., 2016). Therefore, the observed radiant flux per area over all wavelengths is written as follows:

$$F(T) = \pi \int_0^\infty \epsilon(\lambda) B(\lambda, T) R(\lambda) d\lambda, \qquad (3)$$

where $\epsilon(\lambda)$ is the spectral thermal emissivity. For simplicity, the approximate thermal emissivity is used for the mean value of ϵ. Figure 2 shows the calculated radiant flux per area emitted from a blackbody ($\epsilon = 1$) and the anticipated flux per area of the TIR for the temperature range of this experiment.

The observed data obtained using the TIR are digital data in analog-to-digital units (ADUs). The data must be transformed to temperatures using a calibration curve. A least-squares fitting allows searching for the best-fit parameters by minimizing the value of χ^2, which is obtained as follows:

$$\chi^2 = \sum_{i=1}^{N} \left(\frac{D_i - D_i'}{S_i} \right)^2, \qquad (4)$$

where D_i is the observed data in ADUs, D_i' is a model parameter related to radiant flux in ADUs, S_i is the standard deviation of the observed data in ADUs, and i denotes the measurement number (where measurements are taken at target temperatures of 30 to 100°C in 5°C increments), and N is the number of degrees of freedom (= 15). Linear dependence is assumed between the values of the model parameter and the radiant flux per area emitted from targets obtained using Eq. (3):

$$D_i' = p_1 \times F(T_i) + p_2, \qquad (5)$$

where p_1 and p_2 are set as free parameters in the fitting. The parameter p_1 is the conversion coefficient from radiant flux to a digital value, and p_2 is the dark offset. These parameters are determined approximately by the fitting using the Levenberg-Marquardt method (Press et al., 2007a). The reduced χ^2 (sum of squares of residuals/degree of freedom) and the p-value (probability of exceeding χ^2) are indicators of the goodness of fit (Bevington and Robinson, 2002). A linear interpolation method (Press et al., 2007b) can approximately derive the temperature T from the radiant flux F by inverse conversion.

2.3 Results

The observed data and the best-fit calibration curve are shown in Fig. 3. The best-fit parameters of Eq. (5) are $p_1 = 3.24 \pm 0.01$ and $p_2 = -314.72 \pm 0.97$ (reduced $\chi^2 = 1.58$, p-value=0.08). Thus, the calibration curve is rewritten as follows:

$$D' = 3.24 \times F(T + 273.15) - 314.72. \tag{6}$$

This calibration curve allows for the conversion of observed digital data to target temperature within an error of 1˚C (3σ), as shown in Fig. 3. The above result indicates that one digital unit equivalent to a temperature of 0.16˚C at the target temperature of 50.0˚C, which is regarded as the temperature resolution of the TIR. This result was measured under atmospheric conditions, and the calibration curve depended on the surrounding temperature. Therefore, in the future, the calibration curve for transforming absolute temperature must be reconstructed for the asteroid observation using prelaunch data obtained in a vacuum chamber.

3 Evaluation using a known thermal emissivity target

The purpose of this evaluation of the TIR is to clarify the accuracy of the calibration curve obtained through the calibration test by measuring a known thermal emissivity target using the TIR.

3.1 Thermal emissivity of black almite

The observed temperature varies depending on the surface thermal emissivity of the target, and thus a known thermal emissivity target is required in order to evaluate the imaging performance of the TIR. A sandblasted black almite plate (30 mm × 30 mm, thickness: 1 mm) was prepared as the known thermal emissivity target. The spectral profile of this plate was measured by Fourier transform infrared (FT-IR) spectroscopy (VERTEX 70 Bruker Optics). Figure 4 shows the spectral reflectance of the plate as measured using the FT-IR. The thermal emissivity was calculated using Kirchhoff's law of thermal radiation (1-

reflectance). The resulting mean thermal emissivity ε was 0.96±0.01 for the wavelength range of 8 to 12 μm.

3.2 Experimental configuration

This evaluation was performed using a large-aperture collimator. The configuration was the same as that used in the calibration test, as shown schematically in Fig. 5. A round heater (Minco flexible heater, diameter: 48 mm, 78 Ohm) was affixed to the back of an aluminum plate holder. The heater was continuously controlled by a proportional integrated derivative (PID) method using a digital controller (OMRON). A black almite plate was mounted on the aluminum holder and was warmed by the heater. The temperatures of the black almite plate and the aluminum holder were measured using type K thermo-couples. A gap between the plate and the holder was filled by inserting pieces of aluminum foil. The surrounding temperature was approximately 20°C.

3.3 Results

The TIR captured thermal images of the black almite plate at target temperatures of 35.0°C, 42.5°C, and 50.0°C. Figure 6 shows a photograph of the black almite, as well as the mean thermal image and its corresponding standard deviation image (16 frames of a 128-frame stack), captured using the TIR at 50.0°C. The observed temperature of the thermal image was calculated using Eq. (6). The standard deviation for the continuous shooting of 16 frames included random errors of the observed temperature, which was less than 0.3°C (1σ) for every pixel at 50.0°C (Fig. 6b).

The temperature of the black almite plate observed using the TIR (Fig. 7), which was converted using the calibration curve obtained through the calibration test, is consistent with the temperature measured using the type K thermocouples with an error of approximately 1°C (3σ). Therefore, the TIR can determine the actual temperature of the target based on the observed temperature if the thermal emissivity of the target is known. However, the temperatures determined using the thermocouples were slightly higher than those measured using the TIR. The thermocouples were affixed to the black almite plate using polyimide tape, and thus differences in thermal emissivity might cause temperature differences.

4 Demonstration using Carbonaceous chondrites

The purpose of the demonstration is to measure the asteroid analogs and to practice thermal imaging for the asteroid observation of the TIR.

4.1 Meteorite samples

The Hayabusa2 target asteroid is Ryugu, a C-type asteroid that appears to consist of hydrated and dehydrated carbonaceous chondrite materials, and so carbonaceous chondrite measurements demonstrate the ability of the TIR in the asteroid observation. In the present study, three CM carbonaceous chondrites (Murray, Jbilet Winselwan, and Murchison) were measured using the TIR, which was prepared for calibration of the near-infrared spectrometer on- board Hayabusa2 (NIRS3) (Iwata et al., 2016; Nakamura et al., 2015). These meteorites are classified as petrologic type CM2 (Schmus and Wood, 1967; Weisberg et al., 2006). One of the three samples, Jbilet Winselwan, was heated and partially dehydrated (Nakamura et al., 2015) and had a large crack (Fig. 8b.1). The telescopic optical navigation camera (ONC-T) of Hayabusa2 has detected an absorption feature of the 0.7 μm band, which is indicative of the presence of hydrous silicate Fe-rich serpentine, from Murchison and Mur- ray, but not from Jbilet Winselwan, because of decomposition of serpentine (Kameda et al., 2015). Spectral profiles of all three meteorites were obtained using FT-IR for various phase angles, particle sizes, and temperatures (Nakamura et al., 2015). The mean thermal emissivity ε of the meteorites considered the experiment of the present study was approximately 0.98 for the wavelength range of 8 to 12 μm. The same meteorites were observed using the NIRS3, the ONC, and the TIR were used for cross-calibration (Okada et al., 2014).

4.2 Meteorite experiment configuration

The configuration of the demonstration using the meteorites was the same as that used in the evaluation using the black almite plate (Fig. 5). The meteorites, which were mounted on the sample holder, were warmed from the back using the heater. The temperature was varied by the PID method using the digital controller. The TIR captured thermal images of the surface meteorites at temperatures of 35.0°C, 42.5°C, and 50.0°C.

4.3 Results

Figure 8 shows photographs of the three carbonaceous chondrites (Murray, Jbilet Winselwan, and Murchison) along with corresponding thermal images captured using the TIR at 50.0°C. Areas of slightly lower temperature appear in the thermal image of Murray (Fig. 8a.2). These areas are not chondrules, but

rather small pits in the surface (shown in white) (Fig. 8a.1). The temperatures of these areas were approximately 2°C lower than the surrounding temperature (Fig. 8a.2). A large crack appears in the thermal image of Jbilet Winselwan (Fig. 8b.1), and this crack is also a low-temperature area (Fig. 8b.2). The temperature was approximately 3°C lower than the surrounding surface temperature. The surface temperature of Murchison is featureless, as compared with the other meteorites (Fig. 8c.2).

5 Discussion

5.1 Thermal emissivity and surface roughness of meteorites

The thermal emissivity of the carbonaceous chondrite was mostly black ($\varepsilon \sim= 0.98$), although the surface roughness causes variations in the temperature measured by the TIR. The spatially local difference in the surface temperature varied between 45 to 47°C in the thermal image of the Murray meteorite. Using Eq. (2), this difference is equivalent to a difference in thermal emissivity ε of 0.98 to 0.90 and surface roughness variations at a surrounding temperature of 20°C, as follows:

$$0.90 \times \sigma((47 + 273)^4 - (20 + 273)^4) \cong 0.98 \times \sigma((45 + 273)^4 - (20 + 273)^4).$$

In general, the area of small particle size is a high-albedo area. The albedo increases with decreasing particle size in the visible and near-infrared observations (Adams and Filice, 1967). Therefore, areas such as the pit of the Murray meteorite might exhibit decreased thermal emissivity, as well as surface roughness. In laboratory experiments, estimating the actual thermal emissivity and surface roughness of several asteroid analogs using a thermostatic chamber is required in order to establish a uniform temperature distribution for future research.

Figure 9a shows the temperature of the Jbilet Winselwan meteorite as measured by the type K thermocouples and the calculated temperature for stepper thermal emissivity changes $\Delta\varepsilon$ of 0.02 around the measured temperature. Points A and B show the temperature measured by the TIR (Fig. 8b.2). These anticipated temperatures indicate that TIR allows for determining the thermal emissivity distribution of the asteroid surface within an accuracy of $\Delta\varepsilon \sim= 0.02$ because the error bars of temperatures measured using the TIR are smaller than the calculated temperature for thermal emissivity changes $\Delta\varepsilon$ of 0.02.

5.2 Thermal inertia of meteorites

Here, a heat balance model is considered in the meteorite experiments in or- der to estimate the thermal inertia of meteorites. The heat balance model is assumed to be simply written as a one-dimensional finite model, as described in Appendix A. In the model, the specific heat c_p was assumed to be 600 $Jkg^{-1}K^{-1}$ (Yomogida and Matsui, 1983), and the density ρ was assumed to be the apparent density estimated based on the volume and weight, 2,440 kgm^{-3} (thickness: 2.4 mm). A least-squares fitting was performed for 251 points in the time range of 1,490 to 3,990 s. The parameters were the thermal conductivity κ and the convective heat transfer coefficient H. In this case; the best-fit values were $\kappa = 0.48 \pm 0.04$ and $H = 120.9 \pm 10.7$. The resulting value of H was large because heat loss occurred in unsteady state measurements. Hence, the resulting thermal inertia was $\Gamma=839$ $Jm^{-2}s^{0.5}K^{-1}$, calculated by Eq. (1). This value of the thermal inertia is slightly larger than that of Cold Bokkeveld (CM2) reported by Opeil et al. (2010), $\Gamma=645$ $Jm^{-2}s^{0.5}K^{-1}$ and $\kappa = 0.5$ $(Wm^{-1}K^{-1})$ at 200 (K), because of the different density and heat capacity values. An example of the temperature profile of the Jbilet Winselwan meteorite, measured by the type K thermocouples and the TIR, is shown in Fig. 9. Here, the temperature profiles change with the value of the thermal inertia, as simulated by the heat model, in steps of $\Delta\Gamma = 20$ $Jm^{-2}s^{0.5}K^{-1}$ around the best-fit temperature profile (Fig. 9b).

The lowest temperature area in the thermal image of the Jbilet Winselwan meteorite was the crack (Fig. 8b.2), where the temperature was approximately 3°C lower than the temperature of the surrounding area. The heat model indicates that the 3°C temperature difference was caused by the difference in thermal inertia of approximately $\Delta\Gamma = 150$ $Jm^{-2}s^{0.5}K^{-1}$ on the meteorite (Fig. 9b). The TIR will resolve the thermal inertia distribution on the asteroid surface within an accuracy of $\Delta\Gamma \sim= 20$ $Jm^{-2}s^{0.5}K^{-1}$ because the error bars of temperatures measured using the TIR are smaller than the steps of simulated temperature profiles.

5.3 Asteroid observation

The TIR will observe the same area of the asteroid surface several times (> 10 times, in order to ensure statistical significance) and will take the surface thermal emissivity and thermal inertia parameters into account by a least-squares fitting of a thermal model. Recently, thermophysical models of asteroids have been developed and updated (Spencer et al., 1989; Müller, 2007; Delbo et al., 2015), and the thermal model for the Ryugu observation by the TIR is also being improved (Takita et al., 2016).

The physical properties of the asteroid surface are unknown. For instance, a crater ray on the lunar surface creates a compositional contrast between the high-albedo ejecta and the surrounding mature terrain (Hawke et al. 2004). If similar yet smaller ejecta on the surface of an asteroid change the surface thermal emissivity, the temperature observed using the TIR will vary. Therefore, the TIR will find characteristic areas of the surface of the asteroid by measuring temperature variation. Moreover, the particle sizes of the surface layer may be constrained by estimating the thermal inertia, as has been investigated in laboratory experiments for regolith analogs (Sakatani et al., 2012).

The surface layer of Ryugu may be composed of a regolith and pebble rock mixture, as anticipated by ground-based telescope and space-based telescope observations. The thermal properties of the mixture targets must be determined. Laboratory experiments will be performed in order to estimate the thermal inertia of a mixture target, such as a slab meteorite or a powdered meteorite.

6 Summary and Future research

Summary

(1) The calibration curve of the TIR, which was constructed by measuring a blackbody source, could determine observed temperatures with an error of less than 1°C (3σ) at target temperatures of 30 to 100°C. (2) The TIR could resolve the temperature variation of a known thermal emissivity target with a random error of 0.3°C for each pixel at a target temperature of 50°C. (3) The thermal imaging performance of the TIR implies that the TIR can observe the spatial distributions of thermal inertia and thermal emissivity of the asteroid surface within accuracies of $\Delta\Gamma \sim= 20$ $Jm^{-2}s^{0.5}K^{-1}$ and $\Delta\varepsilon \sim= 0.02$, respectively. These experiments indicate that the thermal imaging performance of the TIR should be sufficient to perform asteroid observations.

Future research

(1) Distinguishing between the effects of thermal emissivity, surface roughness, and thermal inertia is critical for asteroid observation because these effects locally change the surface temperature. A specific thermal model of Ryugu is being developed in order to derive the actual values of the thermal emissivity and thermal inertia using a least-squares fitting. (2) A priori information obtained through laboratory experiments is required in order to estimate the variations of thermal emissivity and surface roughness for

several asteroid analogs. The estimation must be performed in a thermostatic chamber in order to make the temperature of the target uniform. (3) In order to determine the thermal inertia of a mixture target, such as a slab meteorite or a powdered meteorite, estimation should be performed in a vacuum chamber for observation of the complex surface of an actual asteroid.

Appendix A: Heat balance model for meteorite experiments

The thermal inertia of the meteorites is approximately derived using a heat balance model. The heat flow in the meteorite layer is simply modeled using a one-dimensional, non-steady- state heat transfer equation, as follows:

$$\rho c_p \frac{\partial T(x,t)}{\partial t} = k \frac{\partial^2 T(x,t)}{\partial x^2}, \tag{7}$$

where κ is the thermal conductivity $(Wm^{-1}K^{-1})$, c_p is the specific heat $(J\,kg^{-1}K^{-1})$, and ρ is the density $(kg\,m^{-3})$. The initial temperature is set to room temperature, and the boundary condition is obtained based on the heat balance of the Fourier equation, the Stefan-Boltzmann law, and the convective heat for the surroundings, as shown in Fig. 10. The boundary condition is written as follows:

$$-\kappa \left(\frac{\partial T(x,t)}{\partial x} \right)_{x=x_0} = q(x_0, t) \tag{8}$$

$$-\kappa \left(\frac{\partial T(x,t)}{\partial x} \right)_{x=x_N} = \epsilon\sigma (T(x_N,t)^4 - T(\infty,t)^4) + H(T(x_N,t) - T(\infty,t)),$$

where $q(x_0,t)$ is the heat flux supplied from the heater to the back side of the meteorite (Wm^{-2}), $T(\infty,t)$ is the surrounding temperature (K), and H is the convective heat transfer coefficient $(Wm^{-2}K^{-1})$. The heated layer is set as the back side of meteorite $(x = x_0)$, and the imaging layer of the TIR is the front side of the meteorite specimen $(x = x_N)$. Indexes 0 through N indicate the layer number. A 20-layer model is used in this calculation. The unknown parameters of the equations are κ and H. The convective heat is dominant under these conditions (atmospheric conditions). The spatial variation of thermal emissivity is assumed to be negligible, and the value of thermal emissivity ε is assumed to be constant at 0.98.

The heat balance equation can be approximately solved using a numerical finite difference method (implicit method) (Crank and Nicolson, 1947; Press et al., 2007c). The variance of this finite difference equation becomes a quartic equation of temperature $T(x_N)$.

This quartic equation can be solved using a classical quartic formula of the Ferrari method (Cardano's formula). Equations (7) and (8) are fitted to the measured temperature with the thermocouple data by least-squares fitting. The free parameters are κ and H, and the value of c_p is assumed to be constant.

Fig. 10 Schematic diagram of the one-dimensional heat balance model of the warmed meteorite. The meteorites were warmed from the back side of the specimen using a heater. The heat balance boundaries were the meteorite surface ($x = x_N$) and the heated layer ($x = x_0$). The temperatures at these boundaries were measured using type K thermocouples. In the present study, a non-steady heat balance equation was approximately solved for 20 layers using a numerical finite difference method (implicit method).

References

J.B. Adams, A.L. Filice, Spectral reflectance 0.4 to 2.0 microns of silicate powders, J. Geo- phys. Res., 72, 5705–5715 (1967)

A.M. Baldridge, S.J. HooK , C.I. Grove, G. Rivera, The ASTER spectral library version 2.0, Remote Sensing of Environment, 113, 711–715 (2009)

P.R. Bevington and D.K. Robinson, Data Reduction and Error Analysis for the Physical Sciences, 3rd Ed, McGraw-Hill (2002)

W.F. Bottke, Jr., D. Vokrouhlicky´, D.P. Rubincam, D. Nesvorny´, The Yarkovsky and YORP Effects: Implications for Asteroid Dynamics, Annu. Rev. Earth Planet. Sci., 34, 157–191 (2006)

S.J. Bus and R.P. Binzel, Phase II of the Small Main-Belt Asteroid Spectroscopic Survey. A Feature-Based Taxonomy, Icarus, 158 1, 146–177 (2002)

H. Campins, J. P. Emery, M. Kelley, Y. Fern´andez, J. Licandro, M. Delbo´, A. Barucci, and E. Dotto, Spitzer observations of spacecraft target 162173 (1999 JU$_3$), A&A, 503, L17-L20 (2009)

J. Crank and P. Nicolson, A practical method for numerical evaluation of solutions of partial differential equations of the heat-conduction type, Proc. Camb. Phil. Soc., 43, 50–67 (1947)

M. Delbo, M. Mueller, J. P. Emery, B. Rozitis, M. T. Capria, Asteroid thermophysical modeling, in Asteroids IV (ads. P. Michel et al.), Univ. of Arizona Press, 107–128 (2015)

T. Fukuhara, M Taguchi, T. Imamura, M. Nakamura, M. Ueno, M. Suzuki, N. Iwagami, M. Sato, K. Mitsuyama, G. L. Hashimoto, R. Ohshima, T. Kouyama, H. Ando, and M. Futaguchi, LIR: Longwave Infrared Camera onboard the Venus orbiter Akatsuki, Earth Planets Space, 63, 1009–1018 (2011)

S. Hasegawa, T. G. Müller, K. Kawakami, T. Kasuga, T. Wada, Y. Ita, N. Takato, H. Terada, T. Fujiyoshi, M. Abe, Albedo, Size, and Surface Characteristics of Hayabusa-2 Sample-Return Target 162173 1999 JU_3 from AKARI and Subaru Observations, Publ. Astron. Soc. Japan, 60, 399–405 (2008)

B.R. Hawke, D.T. Blewett, P.G. Lucey, G.A. Smith, J.F. Bell III, B.A. Campbell, M.S. Robinson, The origin of lunar crater rays, Icarus, 170, 1–16 (2004)

T. Iwata, K. Kitazato, M. Abe, M. Ohtake, T. Arai, T. Arai, N. Hirata, T. Hiroi, C. Honda, N. Imae, M. Komatsu, T. Matsunaga, M. Matsuoka, S. Matsuura, T. Nakamura, A. Nakato, Y. Nakauchi, T. Osawa, H. Senshu, Y. Takagi, K. Tsumura, N. Takato, S. Watanabe, M. A. Barucci, E. Palomba, M. Ozaki, NIRS3: The Near Infrared Spectrometer on Hayabusa2, Space Sci. Rev. (2016, this issue)

S. Kameda, H. Suzuki, Y. Cho, S. Koga, M. Yamada, T. Nakamura, T. Hiroi, H. Sawada,

R. Honda, T. Morota, C. Honda, A. Takei, T. Takamatsu, Y. Okumura, M. Sato, T. Yasuda, K. Shibasaki, S. Ikezawa, S. Sugita, Detectability of hydrous minerals using ONC-T camera onboard the Hayabusa2 spacecraft, ASR (2015).

D. Lazzaro, M.A. Barucci, D. Perna, F.L. Jasmim, M. Yoshikawa, and J.M.F. Carvano, Rotational spectra of (162173) 1999 JU_3, the target of the Hayabusa2 mission, A&A, 549, L2 (2013)

M. Müller, Surface Properties of Asteroids from Mid-Infrared Observations and Thermo- physical Modeling, PhD dissertation, Freie Universitaet Berlin (2007)

T.G. Müller, J. Durech, S. Hasegawa, M. Abe, K. Kawakami, T. Kasuga, D. Kinoshita, D. Kuroda, S. Urakawa, S. Okumura, Y. Sarugaku, S. Miyasaka, Y. Takagi, P. R. Weissman, Y. -J. Choi, S. Larson, K. Yanagisawa and S. Nagayama, Thermo-physical properties of 162173 (1999 JU_3), a potential flyby and rendezvous target for interplanetary missions, A&A, 525, A145 (2011)

T. Nakamura, T. Iwata, K. Kitasato, M. Abe, T. Osawa, M. Matsuoka, Y. Nakauchi, T. Arai, M. Komatsu, T. Hiroi, N. Imae, A. Yamaguchi, H. Kojima, Reflectance Spectra Measurement of Various Carbonaceous Chondrites Using Hayabusa-2 Near Infrared Spectrometer, 78th Annual Meeting of the Meteoritical Society, abstrct#5206 (2015)

T. Okada, T. Iwata, Near Infrared Spectroscopy and Thermal Infrared Imagery on Hayabusa2: Hydrated and Physical State of C-Class Asteroid 1999 JU$_3$, New Results in the Observations and Space Exploration of Asteroids, in Proceedings of An International CJMT-1 Workshop on Asteroidal Science, October 16-17, 2012, Macao, eds: W. Ip, 97–112 (2014)

T. Okada, T. Fukuhara, S. Tanaka, M. Taguchi, T. Imamura, T. Arai, H. Senshu, Y. Ogawa, H. Demura, K. Kitazato, R. Nakamura, T. Kouyama, T. Sekiguchi, S. Hasegawa, T. Matsunaga, T. Wada, J. Takita, N. Sakatani, Y. Horikawa, K. Endo, J. Helbert, T. G. Mu゛ller, A. Hagermann, Hayabusa2 TIR team, Thermal Infrared Imaging Experiments of C-Type Asteroid 162173 Ryugu on Hayabusa2, Space Sci. Rev. (2016, this issue)

C.P. Opeil, G.J. Consolmagno, D.T. Britt, The thermal conductivity of meteorites: New measurements and analysis, Icarus, 208 1, 449-454 (2010)

W.H. Press, S.A. Teukolsky, W.T. Vetterling, B.P. Flannery, Chapter 15, Modeling of Data, Numerical Recipes, Third Edition, Cambridge University Press, 773–839 (2007)

W.H. Press, S.A. Teukolsky, W.T. Vetterling, B.P. Flannery, Chapter 3, Interpolation and Extrapolation, Numerical Recipes, Third Edition, Cambridge University Press, 110–154 (2007)

W.H. Press, S.A. Teukolsky, W.T. Vetterling, B.P. Flannery, Chapter 20, Partial Differential Equations, Numerical Recipes, Third Edition, Cambridge University Press, 1024–1096 (2007)

B. Rozitis and S. F. Green, Directional characteristics of thermal-infrared beaming from atmosphereless planetary surfaces - a new thermophysical model, MNRAS, 415, 2042– 2062 (2011)

N. Sakatani, K. Ogawa, Y. Iijima, R. Honda, S. Tanaka, Experimental study for thermal conductivity structure of lunar surface regolith: Effect of compressional stress, Icarus, 221 2, 1180–1182 (2012)

W.R. Van Schmus, J. A. Wood, A chemical-petrologic classification for the chondritic meteorites, GCA, 31 5, 747 (1967)

J.R. Spencer, L. A. Lebovsky, M. A. Sykes, Systematic biases in radiometric diameter de- terminations, Icarus, 78, 337–354 (1989)

J. Takita, H. Senshu, S. Tanaka, Feasibility and accuracy of thermophysical estimation of asteroid 162173 Ryugu (1999 JU$_3$) from the Hayabusa2 Thermal Infrared Imager, Space Sci. Rev. (2016, this issue)

Y. Tsuda, M. Yoshikawa, M. Abe, H. Minamino, S. Nakazawa, System design of the Hayabusa 2–Asteroid sample return mission to 1999 JU$_3$, Acta Astronautica, 91, 356– 362 (2013)

F. Vilas, Spectral Characteristics of Hayabusa 2 Near-Earth Asteroid Targets 162173 1999 JU$_3$ and 2001 QC34, AJ, 135, 1101–1105 (2008)

M.K. Weisberg, T. J. McCoy, A. N. Krot, Systematics and Evaluation of Meteorite Classification, METEORITES AND THE EARLY SOLAR SYSTEM II, Edited by D. S. Lauretta and H. Y. McSween, THE UNIVERSITY OF ARIZONA PRESS (2006)

K. Yomogida, T. Matsui, Physical properties of ordinary chondrites, J. Geophys. Res., 88, 9513–9533 (1983)

Brucker Optics, http://www.bruker.jp/

CI Systems, http://www.ci-systems.com/ Nippon Avionics, http://www.avio.co.jp/english/
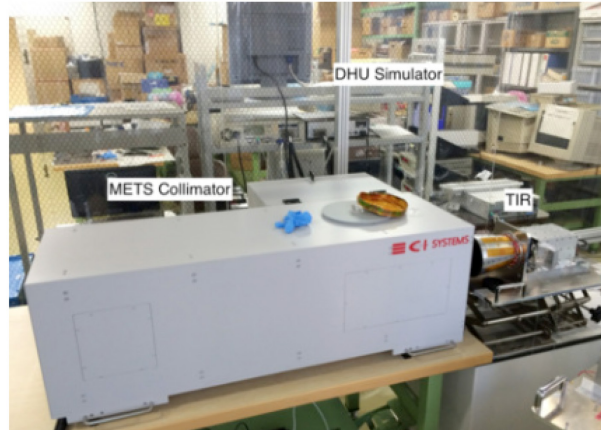
Fig. 1 Experimental setup of the TIR performance test using a large-aperture collimator (METS-VS-8-2.9) under atmospheric conditions. A blackbody source (SR800), a black almite plate, and carbonaceous chondrites were measured using the TIR. The collimator produces the best-focused images because the inner curved mirror generates target figures focused at infinity. The digital electronics of Hayabusa2 were simulated by a data handling unit (DHU) simulator for telemetry and command simulation using the TIR.
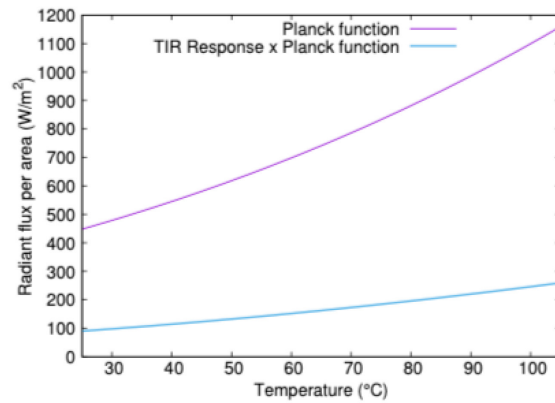
Fig. 2 Radiant flux per area emitted from a blackbody (ϵ=1) and the anticipated flux per are of the TIR calculated using Eq. (3) versus temperature. The blue curve is used as a specific model for the calibration curve of the TIR (Fig. 3).
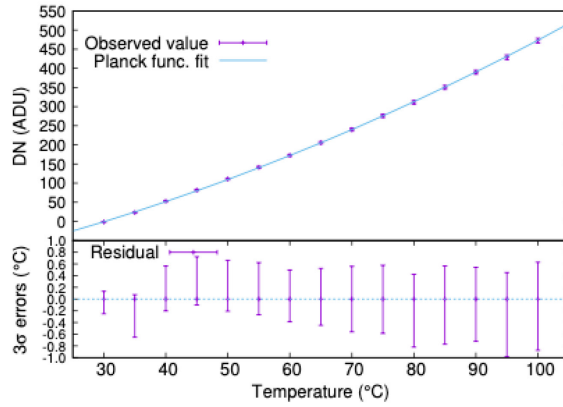
Fig. 3 Observed digital data (obtained using an analog-to-digital unit) and the resulting calibration curve versus target temperature relationship. The data plot shows the mean values of the image center of 100 pixels and the error bars represent 3σ. The line is the best-fit calibration curve fitted using the Planck function model based on Eq. (3) (reduced $\chi^2 = 1.58$, p-value=0.08).
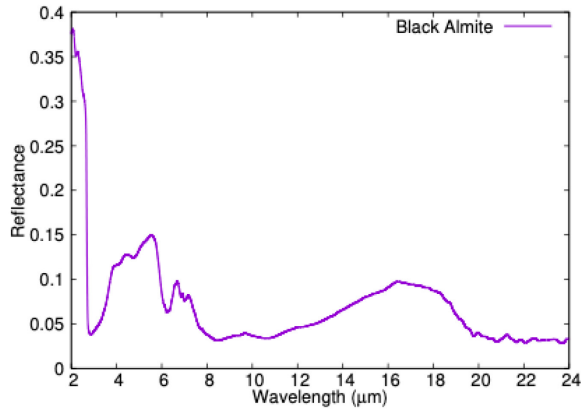
Fig. 4 Spectral reflectance of a sandblasted black almite plate obtained by FT-IR spectroscopy (VERTEX 70, Bruker Optics). A gold-coated target with diffuse reflectance was used as a standard target. The mean thermal emissivity ϵ, as calculated using Kirchhoff's law, was 0.96±0.01 for the wavelength range of 8 to 12 μm.
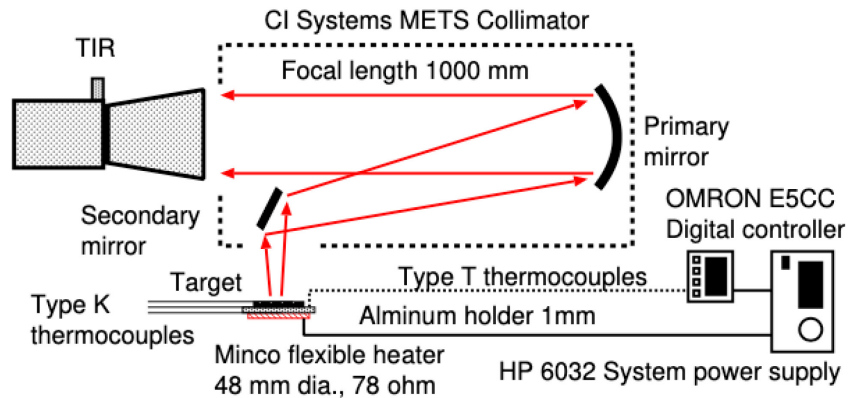
Fig. 5 Schematic diagram of the evaluation performed using a large-aperture collimator. The target was a sandblasted black almite plate (30 mm × 30 mm, thickness: 1 mm). A round flexible heater (Minco, diameter: 48 mm, 78 Ohm) was affixed to the back of an aluminum holder. The heater temperature was controlled by a proportional integral derivative (PID) method using a digital controller (OMRON). The temperatures of the black almite plate and the aluminum holder were measured using type K thermocouples affixed to the front and back of the target and the aluminum plate by polyimide tape.

a. Black almite plate (Picture)   **b.** Black almite plate (TIR thermal image)
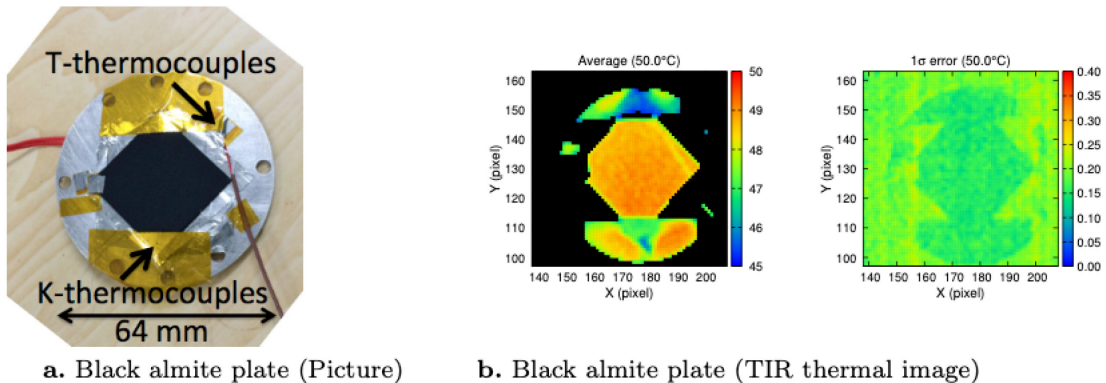
Fig. 6 (a) Photograph of the black almite plate and (b) thermal images captured by the TIR at 50.0°C. The brown cable is connected to a type T thermocouple that was used to monitor and control the temperature of the aluminum holder by the PID method using a digital controller, and the red cable is the power cable of the heater. The thermal images are (b, left) the mean thermal image and (b, right) the standard deviation image obtained by the continuous shooting of 16 frames. The color bars indicate the temperature and standard deviation of temperature in degrees Celsius. The type K thermocouple (thickness: 50 μm) appears in the mean thermal image near $(X,Y)=(190,130)$ (b, left). Mottled patterns remained in the mean image, and thus a flat field correction based on prelaunch data and deep space data collected en route to the asteroid is required in order to reduce the pattern for the asteroid observation.
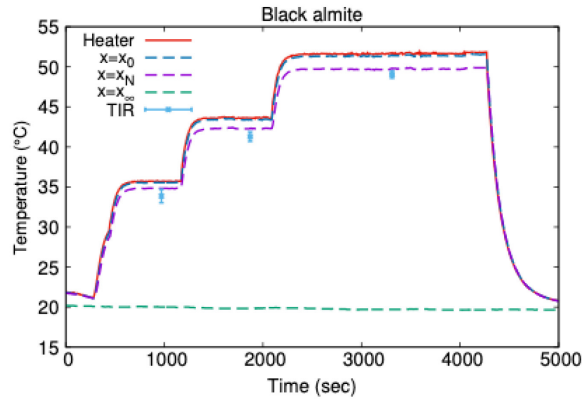
Fig. 7 Temperatures of the black almite plate measured using K-thermocouples and the mean temperature of the temperature measured using the TIR (image center of 10×10 pixels). The red line indicates the heater temperature controlled by the PID method. The setting temperature at the heated area was increased as $35.0°\mathrm{C} \rightarrow 42.5°\mathrm{C} \rightarrow 50.0°\mathrm{C}$. The dotted lines indicate the temperature of the black almite (front: $x = x_N$, back: $x = x_0$) and the surrounding temperature ($x = x_\infty$). The blue plots indicate the temperature observed using the TIR pointing toward the front of the plate. The temperatures measured using the thermocouples and the TIR are consistent with an error of approximately $1°\mathrm{C}$ (3σ).
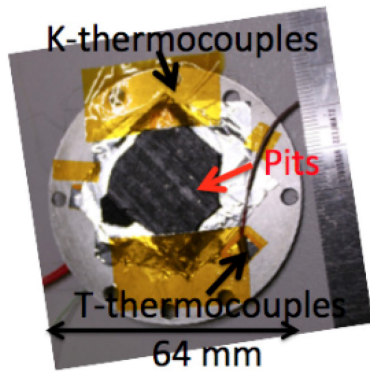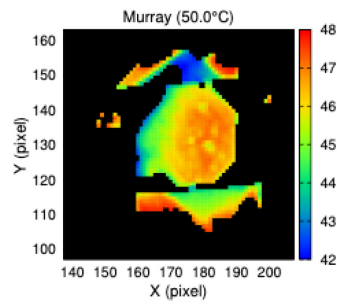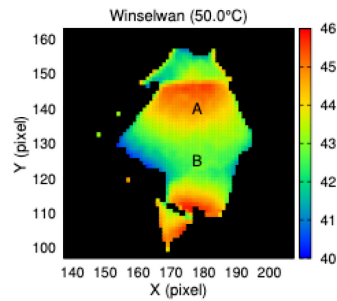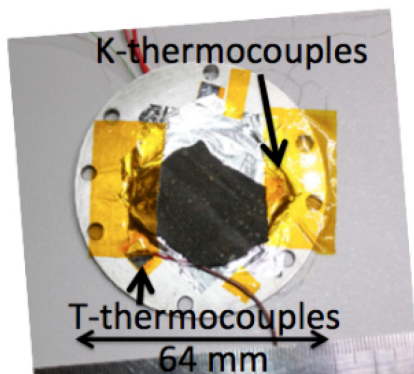
(a.1) Murray Picture

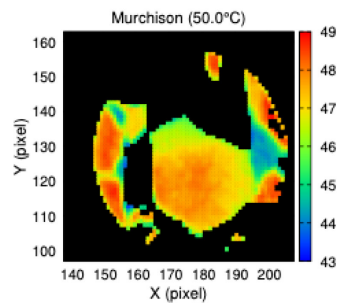**(a.2)** Murray Thermal image (50 °C)
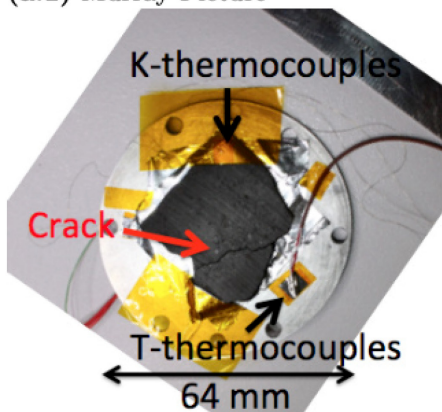
(b.1) Winselwan Picture

(b.2) Winselwan Thermal image (50 °C)

(c.1) Murchison Picture

(c.2) Murchison Thermal image (50 °C)

Fig. 8 Photographs of meteorite samples and corresponding thermal images captured using the TIR at 50.0°C. The color bars indicate the surface temperature in degrees Celsius measured using the TIR. Their thermal images have the spatial distribution of temperature of at most ±3°C. (a.2) Low-temperature areas appear in the thermal image of the Murray meteorite. These areas are caused by small pits in the surface rather than chondrules. The temperature of the pits is approximately 45°C and the temperature of the surrounding area is approximately 47°C. (b.2) In the thermal image of the Jbilet Winselwan meteorite, the large crack is also a low-temperature area. For instance, the temperature at point A is 44.3±0.2°C ($175 \leq X \leq 179$, $135 \leq Y \leq 139$), and the temperature at point B is 42.7±0.2°C ($175 \leq X \leq 179$, $120 \leq Y \leq 124$). (c.2) As shown by the thermal image of the Murchison meteorite, the surface temperature is featureless as compared with the other meteorites.
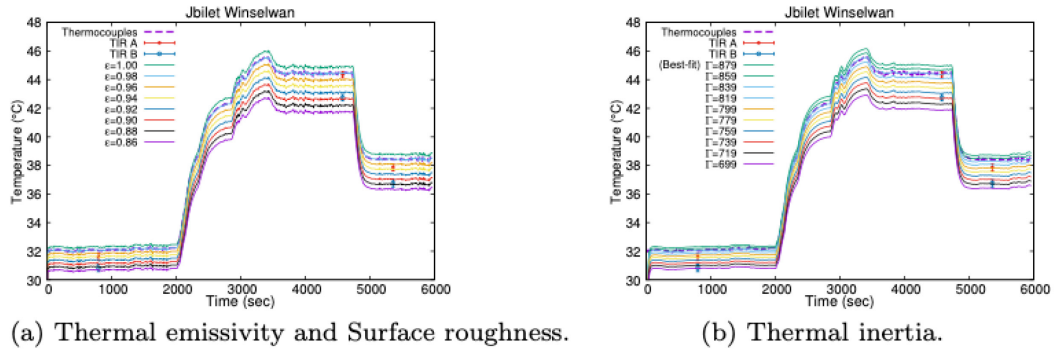
(a) Thermal emissivity and Surface roughness.

(b) Thermal inertia.

Fig. 9 Temperature profiles of the Jbilet Winselwan meteorite measured using type K thermocouples and anticipated temperature profiles for various values of surface thermal emissivity (surface roughness) ϵ calculated by the Stefan-Boltzmann law, and thermal inertia Γ obtained by simulating the heat balance equation. (a) The solid lines indicate the variation in calculated temperature for thermal emissivity steps $\Delta\epsilon$ of 0.02 around the curve measured using the thermocouples. (b) The solid lines indicate the best-fit curves of the heat model described in (Appendix A) for thermal inertia steps $\Delta\Gamma$ of 20 $\mathrm{Jm^{-2}s^{0.5}K^{-1}}$ around the best-fit curve (reduced $\chi^2 = 9.9$, p-value < 0.01). The setting temperature at the heated point was increased as $35.0°\mathrm{C} \to 50.0°\mathrm{C} \to 42.5°\mathrm{C}$. At 3,000 seconds, the distorted curve was manually controlled in order to diminish the rapid temperature change. The TIR captured thermal images of the surface meteorite at three temperatures, indicated as "TIR A" and "TIR B" (Fig. 8b.2).
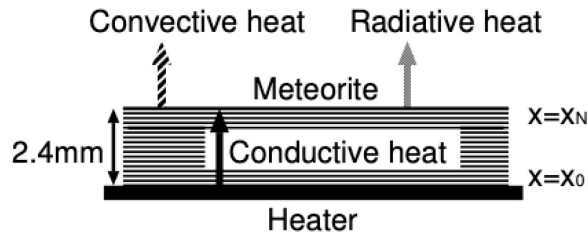

Fig. 10 Schematic diagram of the one-dimensional heat balance model of the warmed meteorite. The meteorites were warmed from the back side of the specimen using a heater. The heat balance boundaries were the meteorite surface ($x = x_N$) and the heated layer ($x = x_0$). The temperatures at these boundaries were measured using type K thermocouples. In the present study, a non-steady heat balance equation was approximately solved for 20 layers using a numerical finite difference method (implicit method).